Data in Brief 44 (2022) 108550

Contents lists available at ScienceDirect

Data in Brief

journal homepage: www.elsevier.com/locate/dib

Data Article

320,000 years of interaction between a fast-spreading ridge and nearby seamounts monitored using major, trace and isotope composition data from oceanic basalts: Zoom at 15.6°N on the East Pacific Rise

Berengere Mougel[a,*], Arnaud Agranier[b], Pascal Gente[b], Christophe Hemond[b]

[a] Centro de Geociencias, UNAM, Querétaro, Mexico
[b] Laboratoire Géosciences Océan, CNRS, IUEM, Université de Brest, UMR 6538, Plouzané, France

ARTICLE INFO

Article history:
Received 23 June 2022
Revised 15 August 2022
Accepted 17 August 2022
Available online 24 August 2022

Keywords:
Mantle geochemistry
Seamounts
Mid-ocean ridge
Radiogenic isotopes
Submersible
High-resolution data

ABSTRACT

Basaltic samples were collected by the French submersible "Nautile" during the "Parisub" cruise (2010, R/V L'Atalante, Ifremer) along a 25 km long sampling profile crossing perpendicularly the current axis of the East Pacific Rise at 15.6°N, as well as the trace of its two former parallel axes located further east. The total length of the profile corresponds to an approximate time interval of ~ 320,000 years. The corresponding dataset documents the geochemical response of Mid-Ocean Ridge Basalts (MORB) related to the progressive convergence between the ridge segment and a nearby hotspot. It also represents one of the highest-sampling (and in turn geochemical) resolution efforts to date. The major, trace element and isotopic compositions determined through optical and mass spectrometry analysis of 52 samples are presented and compared to other previous data obtained from the same area. The data obtained strictly follow the conventions used in rock geochemistry in terms of data acquisition, reduction, and format, so that they can be com-

* Corresponding author.
E-mail address: mougel@geociencias.unam.mx (B. Mougel).

https://doi.org/10.1016/j.dib.2022.108550

pared to similar data from other regions. The different figures present (i) The geological context of study area, (ii) A classification of the samples according to their geochemical composition and geological context for a better legibility of the dataset, (iii) A comparison with data from other oceanic rises, (iv) A detailed method explaining the foundations of the chronology between samples established, and (v) A chronological representation of the geochemical composition of the basalts collected. These data can be useful for anyone interested in marine geosciences and more specifically scientists studying mantle geochemistry, oceanic lithosphere formation, and hotspot-ridge interactions. These data can also be used to model magmatic processes, crust-mantle interactions, and can be integrated in geophysical and geological models of seafloor accretion.

Specifications Table

Subject:	Earth and Planetary Sciences
Specific subject area:	Marine geosciences; mantle geochemistry; oceanic lithosphere formation
Type of data:	Table Image Graph Figure
How the data were acquired:	Basaltic samples (n = 52) were collected by the French submersible "Nautile" during the "Parisub" cruise (2010, R/V L'Atalante, Ifremer) across the EPR axis (15°40′N) between 105°28′W and 105°13′W. Volcanic glass chips were carefully handpicked under a binocular microscope and successively cleaned ultrasonically in both ultra-pure water and ethanol. Following digestion, major and trace element concentrations were obtained *via* an ICP-AES Jovin Yvon Ultima 2 and an HR-ICP-MS Thermo Element II, respectively at the, Pôle Spectrométrie Océan (PSO), Institut Universitaire Européen de la Mer (IUEM) in Brest. Isotopic compositions were obtained from a single digestion (after HCl leaching) of 500–750 mg of sample material. Sr isotopic compositions were analyzed using a Thermo Triton TI-MS, whereas Hf, Nd, and Pb isotope compositions were analyzed using a Thermo Neptune MC-ICP-MS located at, PSO, Ifremer–Brest.
Data format:	Analyzed
Description of data collection:	Raw data were corrected from instrumental mass bias fractionation using exponential mass fractionation laws and the following values for Pb, Sr, Nd, and Hf, respectively: $^{205}Tl/^{203}Tl = 2.388$; $^{88}Sr/^{86}Sr = 8.375202$; $^{146}Nd/^{144}Nd = 0.7219$; and $^{179}Hf/^{177}Hf = 0.7325$. Measured values were compared with international standards globally used for standard bracketing: NIST981: $^{208}Pb/^{204}Pb = 36.7007$, $^{207}Pb/^{204}Pb = 15.4891$, $^{206}Pb/^{204}Pb = 16.9656$; JMC475: $^{176}Hf/^{177}Hf = 0.282157$; LAJOLLA: $^{143}Nd/^{144}Nd = 0.511858$ and JNDI: $^{143}Nd/^{144}Nd = 0.512115$; and NBS987: $^{87}Sr/^{86}Sr = 0.710248$. Accuracy and precision were verified by repeated measurement of these standards during the period of analysis. The standard values obtained were as follows: NBS987 (n = 10): $^{86}Sr/^{87}Sr = 0.710263 \pm 16$ (2sd); JNDI (n = 27): $^{143}Nd/^{144}Nd = 0.512076 \pm 32$ (2sd); LAJOLLA (n = 11): $^{143}Nd/^{144}Nd = 0.511857 \pm 18$ (2sd); NIST981 (n = 23): $^{208}Pb/^{204}Pb = 36.6652 \pm 250$ (2sd), $^{207}Pb/^{204}Pb = 15.4810 \pm 96$

(*continued on next page*)

	(2sd), $^{206}Pb/^{204}Pb$ = 16.9283 ± 86 (2sd); JMC475 (n = 26): $^{176}Hf/^{177}Hf$ = 0.282148 ± 16 (2sd). Additional details are provided in the Experimental design, materials, and methods section.
Data source location:	· East Pacific Rise (15.6°N; -105.4°W) · Pacific Ocean * The coordinates of each of the 52 samples are reported in the data table
Data accessibility:	Data provided in this study are available online at EarthChem https://doi.org/10.26022/IEDA/112071, as well as they are already included in the PetDB database. Secondary data used for comparative purposes are indicated in the figure captions along with the corresponding references from which the data were extracted.
Related research article:	[1] Mougel, B., Agranier, A., Hemond, C., & Gente, P. (2021). High-resolution isotopic variability across EPR segment 16°N: A chronological interpretation of source composition and ridge-seamount interaction. Geochemistry, Geophysics, Geosystems, 22, e2021GC009781. https://doi.org/10.1029/2021GC009781

Value of the Data

- These data are useful to better understand the upper mantle composition, heterogeneity, and history.
- The dataset can provide insights on the temporal and compositional variations of mantle-derived rocks produced at mid-ocean ridge, as well as on the main factors controlling the geochemical variability of rocks from the seafloor.
- These data are useful for anyone interested in marine geosciences, especially scientists studying mantle geochemistry, oceanic lithosphere formation and hotspot-ridge interaction processes.
- These data can be further used to model magmatic processes (e.g., mantle partial melting and melt crystallization), and could be incorporated in more integrative models involving geophysical and geological data.
- The dataset can be directly compared to similar whole-rock geochemical datasets from other regions like those included in the petDB database.

1. Data Description

In this section the data are presented in the form of figures together with their description.

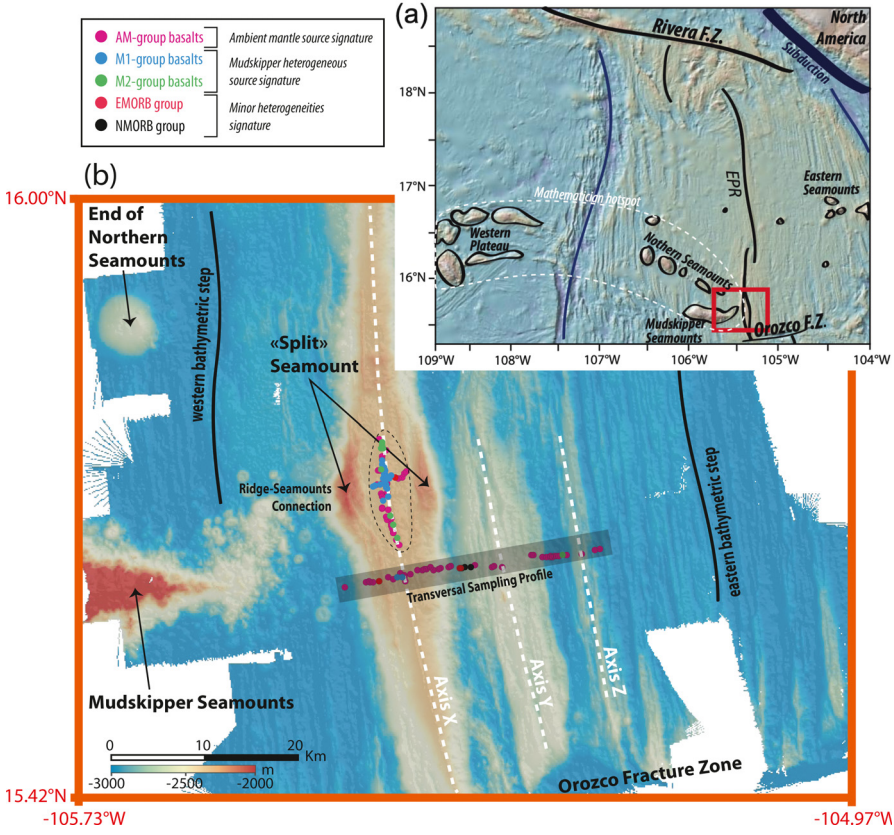

Fig. 1. (adapted [1]): (a) General map presenting the main physiographic features between the Rivera and Orozco Fracture Zones (FZ), and the present study area location (red rectangle). (b) Bathymetry (40 m-grid spacing) of the study area showing the current axis (X) and two relic axes (Y and Z), the "Mudskipper Seamounts" chain, the "Split Seamount" on top of the axis, as well as two high-resolution sampling profiles (axial and transversal). The color code adopted for all samples refers to their "local" isotopic fingerprints. Pink: Ambient Mantle signature (AM); Blue: Mudskipper-type 1 signature (M1); Green: Mudskipper-type 2 signature (M2); Red: Enriched Mid-Ocean Ridge Basalts (E-MORB); Black: depleted Normal Mid-Ocean Ridge Basalt (N-MORB).

Additional comments (Fig. 1): The study area belongs to the history of the northern part of the East Pacific Rise between 10°N and 23°N, and more specifically between the Rivera and the Orozco Fracture Zones (FZ), where the EPR separates the Mathematician Fossil Microplate from the Coco Plate. Between these two fracture zones, the ridge is divided into three second-order segments (Fig. 1a). The two southern segments are separated by a large overlapping spreading

center (OSC) at 16.4°N. The full accretion rate of these two segments is identical (~ 85 mm/a), yet their morphologies differ significantly. The southern segment located between the OSC, and the Orozco fracture zone, and which is the one for which data are reported is on average 300 m shallower and twice wider than the rest of the EPR (Fig. 1b). This singular morphology is due to its interaction with the Mudskipper Seamount Chain located on its western side [2–5]. This chain stands 1000 m above the already very shallow axis of the ridge, and ends in a small recent volcano, symmetrically split by the current ridge axis, and bordering its axial dome. At larger scale, the Mudskipper chain is part of a larger off-axis volcanic complex related to the "Mathematician hotspot" activity, including the "Western Plateau" and the "Northern Seamount Alignment" (Fig. 1a). The current segmentation of the ridge is recent. More than 600,000 years ago this region was composed of three second-order segments and two overlapping spreading centers (OSC), with a smaller central segment. The propagation of the two longer segments led to the elimination of the central segment and the formation of the 16.4°N larger OSC, which is currently migrating towards the South due to the difference in the propagation rate between the two segments.

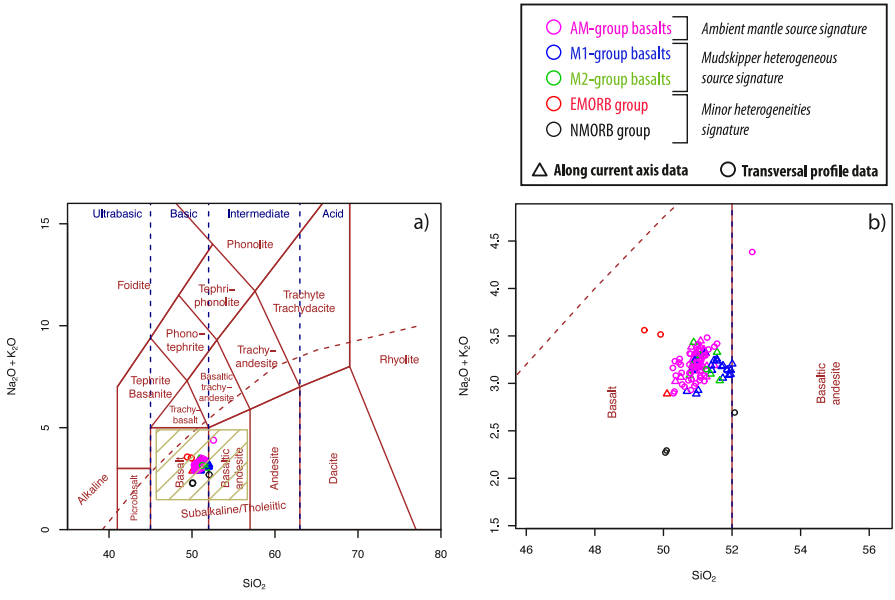

Fig. 2. (a) Total alkalis versus Silica (TAS) diagram for volcanic glasses collected along axis (triangles) and transversal (circles) sampling profiles. (b) Zoom in on the dataset. Triangles and circles correspond to MORB data from the current axial profile [6,7] and from the transversal profile (this work; [1]) respectively. The color code is the same as in Fig. 1. Pink: Ambient Mantle signature (AM); Blue: Mudskipper-type 1 signature (M1); Green: Mudskipper-type 2 signature (M2); Red: Enriched Mid-Ocean Ridge Basalts (E-MORB); Black: depleted Normal Mid-Ocean Ridge Basalt (N-MORB). The distinction between the groups was made based on the of samples' isotopic compositions and trace element patterns specificities.

Additional description (Fig. 2): All samples have low content in alkalis and silica. They plot in the field of basalts, and few samples plot close to the limit between basalt and basaltic andesite. They have relatively homogenous compositions. AM group basalts (pink symbols) is the most

representative group forming a coarse correlation from which depart M1 (blue symbols) and M2 (green symbols) sample groups, which have a relatively higher silica content for a given alkali content. EMORB (red symbols) and NMORB (black symbols) type samples are very few and stand out from other groups with higher and lower alkali contents respectively. They also have among the lowest SiO_2 values (except one sample).

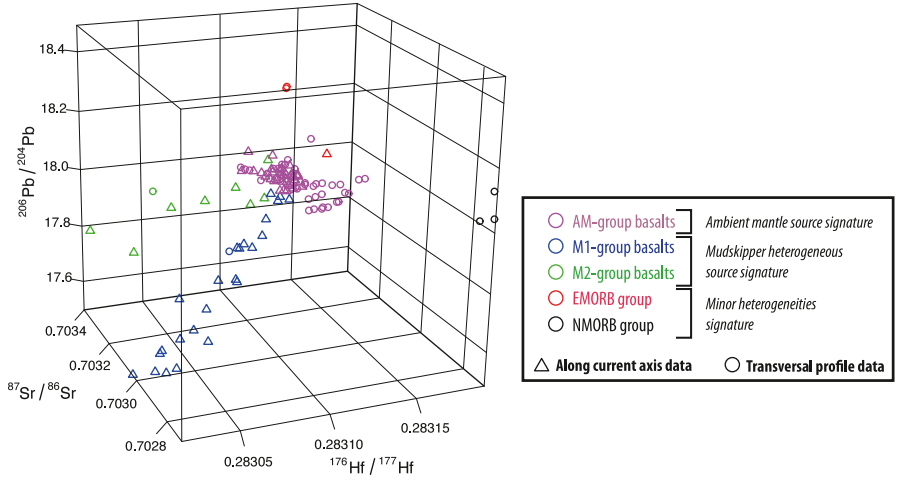

Fig. 3. Samples' 3D isotopic (Sr-Pb-Hf) representation and mantle source discrimination. Triangles and circles correspond to MORB data from the current on-axis profile [6,7] and from the transversal profile, (this work; [1]) respectively. The data are distributed according to three different main trends represented in pink, blue and green. Pink symbols represent the Ambient Mantle trend (AM-group) towards which converge the two other trends. The blue (M1-group) and green (M2-group) symbols are representative of the influence of the Mudskipper Seamounts heterogeneous source on the ridge. EMORB (red) and NMORB (black) samples distinguish themselves from the three main trends and reflect some other minor heterogeneities present within the mantle.

Additional description (Fig. 3): Both blue and green trends trend towards more unradiogenic Pb and Hf and more radiogenic Sr isotopic compositions than the pink trend. However, M2-group (green) has higher $^{87}Sr/^{86}Sr$ ratios for given $^{206}Pb/^{204}Pb$ values than M1-group (blue). N-MORB samples have the lowest Sr, and highest Hf isotopic compositions, while E-MORB samples have the most radiogenic Pb isotope compositions.

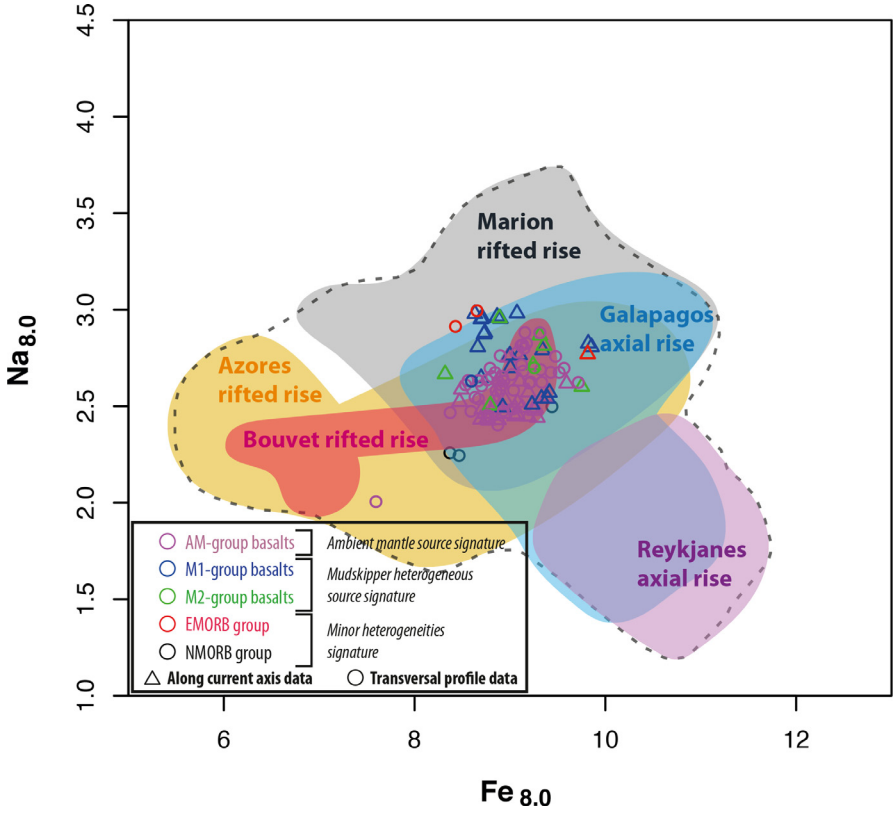

Fig. 4. $Na_{8.0}$ vs. $Fe_{8.0}$ (sodium and iron content corrected for fractionation back to 8.0 wt% MgO) plot for basaltic samples from the study area. Colored fields represent the compositional range of samples from 5 other elevated oceanic rises (Marion in grey; Bouvet in red; Azores in yellow; Galapagos in blue; Reykjanes in purple [8]), excluding outliers.

Additional description (Fig. 4): The whole dataset (transversal and axial profiles) is relatively homogeneous independently of sample groups (i.e., mantle sources variability), and no correlation is observed. However, it can be noticed that on average M1-group basalt and EMORB have higher sodium content, whereas NMORB have both lower sodium and iron contents. Compared to other elevated ridge sections (i.e., ocean rises), samples from the study EPR segment have comparable compositions that plot right in the center of the global oceanic rises field [8].

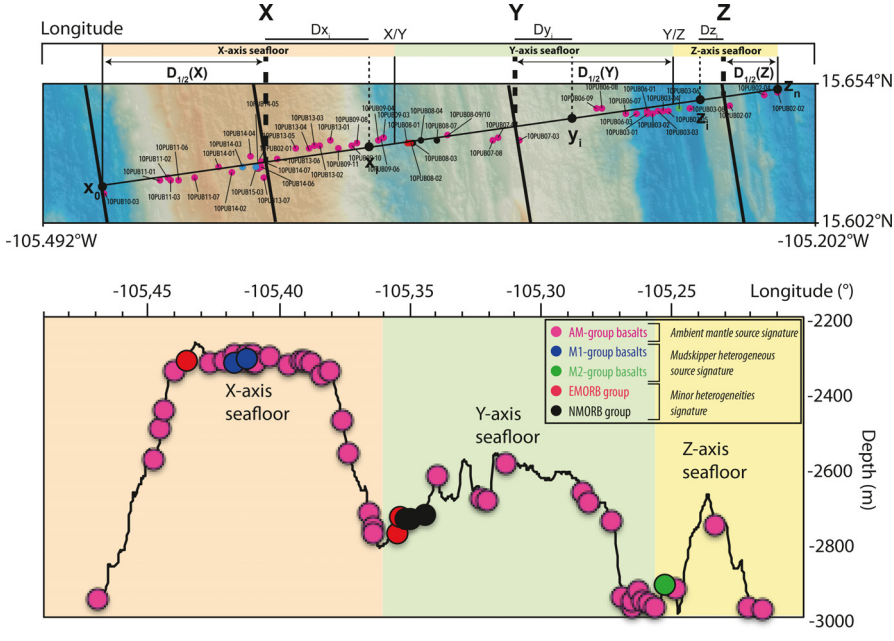

Fig. 5. (adapted from [1])**:** (top) Descriptive sketch of the approach used to establish the relative chronology within the transversal sampling profile. A detailed explanation can be found in the "Experimental design, materials, and methods" section. (bottom) Depth vs. Longitude showing the bathymetric profile of the sampling transect, and the boundaries between the seafloor domains created by the opening of the present axis X (orange), the relic axes Y (green) and Z (yellow). Sample locations are reported on the profile. Samples' color-coding is the same as in previous figures.

Additional description (Fig. 5): $D_{1/2}(X, Y, Z)$ values (°) represent the maximum angular distance produced by each axis X, Y, Z along the transversal sampling profile. x_i, y_i, and z_i designate the samples belonging to the domains created by axes X, Y, Z, respectively. Dx_i,y_i,z_i refer to the angular distance (°) between a sample and its corresponding axis. X/Y and Y/Z represent the apparent geographical limit between the X and Y, and the Y and Z seafloor domains, respectively. The parameters listed above were calculated as follows: $D_{1/2}(X) = |Long(X) - Long(x_0)|$; $D_{1/2}(Y) = |Long(Y) - Long(Y/Z)|$; $D_{1/2}(Z) = |Long(Z) - Long(z_n)|$; $Dx_i = |Long(X) - Long(x_i)|$; $Dy_i = |Long(Y) - Long(y_i)|$; $Dz_i = |Long(Z) - Long(z_i)|$, where Long () refers to the longitude of indicated features in decimal format; z_n and x_0 correspond to the most distant samples from the oldest (Z) and current (X) axes, respectively. N.B. Here the assumption is made that Z and Σz_i are older than Y and Σy_i, which are in turn older than X and Σxi.

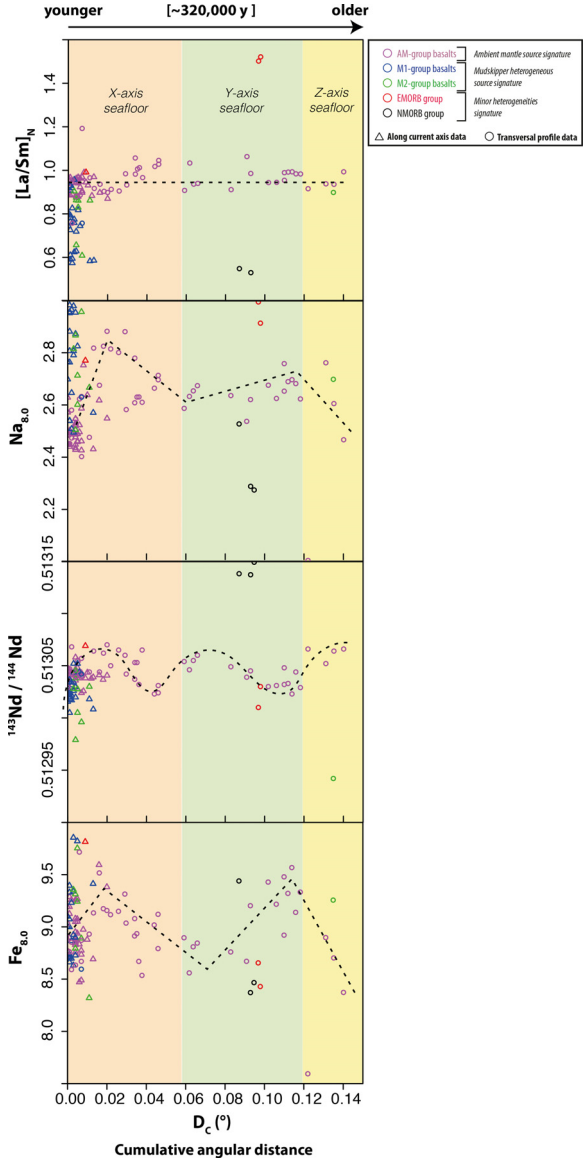

Fig. 6. Left side: $[La/Sm]_N$, $Na_{8.0}$, $^{143}Nd/^{144}Nd$, and $Fe_{8.0}$ vs. Cumulative angular distance Dc (°). La and Sm concentrations have been normalized to primitive mantle [9]. Orange, green, and yellow fields correspond to the seafloor domains opened by the X, Y, and Z axes, respectively. The Dc value for each sample was calculated as follow: $Dc_x = Dx_i$; $Dc_y = D_{1/2}(X) + Dy_i$; $Dc_z = D_{1/2}(X) + D_{1/2}(Y) + Dz_i$. Symbols and colors of all samples are the same as presented in other figures. *The figure should be read as follows: from left to right the higher the Dc value, the older the seafloor is.*

Additional description (Fig. 6): M1 and M2-group basalts (blue and green) show on average more unradiogenic Nd compositions, lower $[La/Sm]_N$ ratios and slightly higher $Na_{8.0}$ compositions than AM-group basalts (pink), whereas $Fe_{8.0}$ compositions are on average relatively uniform irrespectively of basaltic groups. Also note that the reconstructed chronology between samples highlights a characteristic compositional variability among AM-group basalts (pink). While the $[La/Sm]_N$ ratio appears relatively constant around a value of 0.9, the compositions in sodium

and iron of these same samples vary over time forming a sawtooth-shaped curve in the corresponding diagrams. Finally, note that Nd isotope compositions do also show a specific variability for AM-group basalts, forming a sinusoidal curve (T = ∼ 0.05°) of relatively low amplitude.

2. Experimental Design, Materials and Methods

2.1. Rock-Samples Preparation

Fifty-two individual samples of basalts were initially selected based on their location and distribution along the transversal sampling profile, and the presence of fresh glass. The attached glass was first crushed with a hammer into chips, which were then rinsed with distilled water and dried.

The next step consisted in picking manually under binocular ∼ 2 g of the freshest glass chunks for each sample batch. To avoid any cross contamination, the tools were systematically cleaned with water and alcohol between samples. About 1g was used to carry out all the analyses.

2.2. Major Element Analysis

The protocol was adapted from [10].

∼ 250 mg of basaltic glass was digested in a 30 mL Teflon savillex beaker with 4 mL of concentrated HNO_3 – HF mixture during 48 h on a hot plate at 100 ℃. Next, 96 ml of H_3BO_3 aqueous solution (25 g/L H_3BO_3 and 0.5 g/L CsCl) was added to neutralize the excess HF, dissolve the precipitated fluorides, and buffer ionization process during ICP-AES measurement. All reagents were analytical grade. Elements' concentrations were determined from the 100 mL final solution without selective extraction, boron being used as an internal standard. Calibrations were made using international standards CB15, CB18, BELC, JB2 and BEN, which cover the concentration range of the samples to be analyzed. The instrument used for the data acquisition was the ICP-AES Horiba Jobin Ultima 2 of the Pôle Spectrométrie Océan (PSO) located at the Institut Universitaire Européen de la Mer (IUEM), Brest. Relative standard deviations were < 1% for SiO_2 and between 2 and 3% for other major oxides. The data are reported in Table 1.

2.3. Trace Element Analysis

The protocol was adapted from [11].

∼ 50 mg of basaltic glass was weighed (± 10^{-5} g) into a 3 mL Teflon Savillex bomb beaker and digested twice in concentrated HF – $HClO_4$ (at 115 °C), then re-dissolved with 1 mL of concentrated HNO_3 before being finally diluted into 125 mL of 0.5N HNO_3, to which an internal standard of Indium was also added (to yield a concentration of 1 ppb). After one night stabilization, the final solution was measured with the HR-ICP-MS ThermoFinnigan Element II of the PSO at IUEM, Brest. The instrument was calibrated with a 1 ppb multi-elemental solution and monitoring the oxide rate. International rock standards measurements (i.e., BHVO-2; BIR-1; BCR-2) were used for external calibration. Most trace elements were measured in low mass resolution mode, and some (i.e., Sc, V, Co, Zn, Zr, Nb) were analyzed in medium mass resolution mode to resolve isobaric interferences. Relative standard deviations were < 5% for Rare Earth Elements (REE) and systematically < 10% for all other trace elements. The data are reported in Table 2.

2.4. Isotopic analysis

The protocols were adapted from [12,13].

$\sim$ 500–700 mg of basaltic glass was weighed into 7 mL Teflon Savillex beakers. Prior to a 48 h digestion at 120 °C with a concentrated mixture (3:1) of HF-HNO_3, samples were leached with 1 mL 6N HCl during 15 min at 100 °C, followed by 5 min ultrasonification. Then they were re-dissolved with 3 mL of concentrated HF and left for 48 h on a hot plate at 120 °C. At this stage some fluorides form in which Pb and REE are trapped, while Hf remains in solution. Fluorides were then broken *via* 2 h of ultrasonification increasing the total surface reaction and exchange of elements between fluorides and solution. Finally, the solution was centrifugated. The supernatant was used for Hf elution, and the residue left was used for Pb, Sr and Nd separation using chromatographic exchange technique performed in a metal free clean room equipped with Class 100 laminar flow hoods. Hf was eluted *via* a two steps separation process involving HCl, HF and H_2O_2 reactants, and both anionic and cationic exchange resins AG1 $\times$ 8 (100–200 mesh) and AG50WX8 (200–400 mesh), respectively. Because it is the element most likely to be contaminated by anthropogenic inputs, the separation of Pb was performed in a class 1000 clean room dedicated solely to this chemistry using anionic micro-columns containing AG1 $\times$ 8 (200–400 mesh) resin and ultrapure HBr and HCl. This step was repeated twice. The separation of Sr and Nd was performed using specific Eichrom® resins, from the fraction left from Pb elution: (i) Sr Spec (HNO3, warm water) for Sr; (ii) TRU Spec (HNO3) for REE and (iii) LN Spec (HCl) for Nd. All final residues were redissolved in 2% HNO_3 and ready for mass spectrometry (MC-ICP-MS, Neptune). In the case of Sr isotopes measurement (TI-MS; Triton), Sr was deposited on a simple tungsten filament previously degassed under vacuum at 4.5 A on which was also deposited a tantalum activator. The sample was dried at 1.1 A and finally flashed around 4.6 A before introduction into the spectrometer source. Sample blanks recorded insignificant amounts contamination for each element when compared to the total amount of each element isolated from sample material.

The error obtained (2 s.d.) on the isotopic ratios of the entire sample set ($n = 52$) was on average: 7.6.E^{-06} ($\pm$ 4.4) for $^{87}Sr/^{86}Sr$; 5.4.E^{-06} ($\pm$ 5.2) for $^{143}Nd/^{144}Nd$; 5.2.E^{-06} ($\pm$ 3.8) for $^{176}Hf/^{177}Hf$; 1.0.E^{-03} ($\pm$ 0.6 2sd) for $^{206}Pb/^{204}Pb$; 9.9.E^{-04} ($\pm$ 4.6) for $^{207}Pb/^{204}Pb$; and 2.8.E^{-03} ($\pm$ 1.4) for $^{208}Pb/^{204}Pb$. All error bars of individual samples are smaller than the size of the symbols in the corresponding figures.

2.5. Approach Used To Establish A Chronology Between Samples

Usually, at fast spreading ridge, when samples are collected perpendicularly across the ridge axis, the distance of the sample from the axis can be used as a chronological marker between samples (i.e., the more distant it is, the older it is, and vice versa). However, in the study area, previous geophysical studies have shown that the ridge segment jumped twice in the last 300 kyrs (i.e., in the direction of Mudskipper Chain), which resulted in the generation of younger seafloor domains inside older ones due to the relocation of the spreading center. Therefore, a strategy had to be developed to reconstruct the relative chronology among the samples for which geochemical data are presented in this article (Fig. 6).

First, the geographical boundaries between seafloor domains opened by each of the observable axis (X, Y, Z) were determined based on the shape of the bathymetric profile (Fig. 5) corresponding to the sampling transect, as well as the directions of lava flows. Then, the chronology proposed in this work was based on morphotectonic and geophysical observations, whose foundations rely in the following points:

(i) X-axis is the currently active spreading center, Y-axis represents the trace of the preceding extinct axis, and Z-axis represents the trace of the oldest extinct axis.
(ii) At fast spreading centers, melt flux to the axis is high and accretion develops relatively symmetrically compared to slow-spreading oceanic ridges (e.g., [14])

The first point was inferred from previous geophysical studies of the study area [2–5,15,16]. The second point was confirmed by the observation of the symmetrical separation of the “split” seamount over the last 3 kyrs (Fig. 1), as well as repeated evidence of symmetric lava flow

morphology and divergent fronts observed at the Axial Summit Troughs of the 16°N segment [4,17]. Together they allowed us to make the following approximations:

(i) Samples collected in the X-axis seafloor domain are younger than samples collected in the Y-axis seafloor domain, which in turn are younger than samples collected in the Z-axis seafloor domain.
(ii) Inside each seafloor domain, the comparison of angular distance D (°) to the ridge axis between samples determines their relative ages (i.e., the greater, the older)
(iii) Each seafloor domain can be decomposed in 2 symmetrical half-domains with the most extended side $D_{1/2}$ (X, Y, Z) representing the longest time-interval of accretion for each-vaxis within which all the samples' angular distance $D(x_i,y_i,z_i)$ are comprised (irrespective of the half-domain to which they belong).

Then, in order to represent the isotopic composition of each sample as a function of the reconstructed chronology, linearization of the $D(x_i,y_i,z_i)$ values was required to ensure that samples with the same D value, but origin attributed to different axes cannot be confused. Thus, each sample was defined according to a cumulative angular distance D_C (x_i,y_i,z_i) being nothing less than the $D(x_i,y_i,z_i)$ of the sample, to which the corresponding $D_{1/2}(X)$ values for y_i samples and the sum of $D_{1/2}(X)$ and $D_{1/2}(Y)$ for z_i samples were added:

- For samples x_i produced by the currently active X-axis: $Dc_x = Dx_i$.
- For samples y_i produced by the now extinct Y-axis: $Dc_y = D_{1/2}(X) + Dy_i$
- For samples z_i produced by the oldest extinct Z-axis: $Dc_z = D_{1/2}(X) + D_{1/2}(Y) + Dz_i$

Finally, the careful evaluation of lava flow morphologies in the current axial sector, for which high-resolution bathymetric data (1 m in resolution) were available, enabled us to determine the degree of uncertainty for the D value. [17] determined that between 15°37′N and 15°40′N latitude lava flows on average extend over distances $\leq$ 500 m, and in rare occasions reached distances of 1–2 km [4,17], which in turn constitute the uncertainty of the estimated chronology for samples located close to each other.

Ethics Statements

This work does NOT involve human subjects, animal experiments, or data collected from social media platforms.

Declaration of Competing Interest

The authors declare that they have no known competing financial interests or personal relationships that could have appeared to influence the work reported in this paper.

Data Availability

Major, Trace, and radiogenic isotope compositions of basaltic glasses sampled by submersible across the axis of the East Pacific Rise (EPR) 15.6°N (Reference data) (Earth/Chem).

CRediT Author Statement

Berengere Mougel: Conceptualization, Methodology, Validation, Formal analysis, Visualization, Investigation, Writing – original draft, Funding acquisition, Project administration; **Arnaud Agranier:** Conceptualization, Resources, Visualization, Investigation, Writing – review & editing, Funding acquisition, Project administration; **Pascal Gente:** Conceptualization, Investigation, Funding acquisition, Project administration; **Christophe Hemond:** Resources, Investigation, Funding acquisition, Project administration.

Acknowledgments

B. Mougel, A. Agranier, C. Hemond, and P. Gente thank the RV L'Atalante crew and the Nautile team for the great work performed on board during the Cruise Parisub. B. Mougel, A. Agranier, and C. Hemond thank C. Bassoullet, P. Nonnotte, C. Liorzou, E. Ponzevera, and Y. Germain for their help and advice during the analytical work. B. Mougel also thanks M. Le Saout for the interesting discussions about the geological context of the study area.

Funding

This work was financially supported by the grants: CNRS-INSU "PARISUB+"; Institut National des Sciences de l'Univers; Conseil Régional de Bretagne; PAPIIT IA101519 & IA101521, and Conacyt – Ciencia de Frontera N° 26396.

References

[1] B. Mougel, A. Agranier, C. Hemond, P. Gente, High-resolution isotopic variability across EPR segment 16°N: a chronological interpretation of source composition and Ridge–Seamount interaction, Geochem. Geophys. Geosyst. 22 (2021) e2021GC009781, doi:10.1029/2021GC009781.
[2] D.S. Scheirer, K.C. MacDonald, Near-axis seamounts on the flanks of the East Pacific Rise, 8°N to 17°N, J. Geophys. Res. 100 (1995) 2239–2259, doi:10.1029/94JB02769.
[3] S.M. Carbotte, A. Solomon, G. Ponce-Correa, Evaluation of morphological indicators of magma supply and segmentation from a seismic reflection study of the East Pacific Rise 15°30′–17°N, J. Geophys. Res. Solid Earth 105 (2000) 2737–2759, doi:10.1029/1999JB900245.
[4] M.L. Saout, A. Deschamps, S.A. Soule, P. Gente, Segmentation and eruptive activity along the east pacific rise at 16°N, in relation with the nearby mathematician hotspot, Geochem. Geophys. Geosyst. 15 (2014) 4380–4399, doi:10.1002/2014GC005560.
[5] M.L. Saout, R. Thibaud, P. Gente, Detailed analysis of near tectonic features along the East Pacific Rise at 16°N, near the mathematician hot spot, J. Geophys. Res. Solid Earth 123 (2018) 4478–4499, doi:10.1029/2017JB015301.
[6] B. Mougel, A. Agranier, C. Hemond, P. Gente, A highly unradiogenic lead isotopic signature revealed by volcanic rocks from the East Pacific Rise, Nat. Commun. 5 (2014) 4474, doi:10.1038/ncomms5474.
[7] B. Mougel, M. Moreira, A. Agranier, A "high 4He/3He" mantle material detected under the East Pacific Rise (15°4′N), Geophys. Res. Lett. 42 (2015) 1375–1383, doi:10.1002/2014GL062921.
[8] H.J.B. Dick, H. Zhou, Ocean rises are products of variable mantle composition, temperature and focused melting, Nat. Geosci. 8 (2015) 68–74, doi:10.1038/ngeo2318.
[9] W.F. McDonough, S.S. Sun, The composition of the Earth, Chem. Geol. 120 (1995) 223–253, doi:10.1016/0009-2541(94)00140-4.
[10] J. Cotten, A.Le Dez, M. Bau, M. Caroff, R.C. Maury, P. Dulski, S. Fourcade, M. Bohn, R. Brousse, Origin of anomalous rare-earth element and yttrium enrichments in subaerially exposed basalts: evidence from French polynesia, Chem. Geol. 119 (1995) 115–138, doi:10.1016/0009-2541(94)00102-E.
[11] Z.X.A. Li, C.T.A. Lee, Geochemical investigation of serpentinized oceanic lithospheric mantle in the feather river Ophiolite, California: implications for the recycling rate of water by subduction, Chem. Geol. 235 (2006) 161.
[12] J. Blichert-Toft, A. Agranier, M. Andres, R. Kingsley, J.G. Schilling, F. Albarède, Geochemical segmentation of the mid-Atlantic ridge north of Iceland and ridge–hot spot interaction in the North Atlantic, Geochem. Geophys. Geosyst. 6 (2005), doi:10.1029/2004GC000788.
[13] J. Fietzke, A. Eisenhauer, Determination of temperature-dependent stable strontium isotope (88Sr/86Sr) fractionation *via* bracketing standard MC-ICP-MS, Geochem. Geophys. Geosyst. 7 (2006), doi:10.1029/2006GC001243.
[14] R.D. Müller, M. Sdrolias, C. Gaina, W.R. Roest, Age, spreading rates, and spreading asymmetry of the world's ocean crust, Geochem. Geophys. Geosyst. 9 (2008), doi:10.1029/2007GC001743.
[15] A.K. Shah, W.R. Buck, The rise and fall of axial highs during ridge jumps, J. Geophys. Res. Solid Earth 111 (2006), doi:10.1029/2005JB003657.
[16] C.M. Weiland, K.C. Macdonald, Geophysical study of the East Pacific Rise 15°N–17°N: an unusually robust segment, J. Geophys. Res. Solid Earth 101 (1996) 20257–20273, doi:10.1029/96JB01756.
[17] Interaction dorsale-point chaud : relations entre les processus tectoniques et magmatiques à l'axe de la dorsale Est Pacifique, 16°N, PhD (2015) http://www.theses.fr/2015BRES0019/document.